Nanoscale Research Letters

NANO EXPRESS Open Access

Scalable Synthesis Nano-Perovskite $K(Mn_{0.95}Ni_{0.05})F_3$ Cathode by Homogeneous Precipitation Method for Potassium-Ion Batteries

Shuya Wang[1,2], Bin Cui[1*], Quanchao Zhuang[3*], Yueli Shi[3] and Hong Zheng[4]

Abstract

Potassium-ion batteries (KIBs) are favored by researchers because of the unique advantages. In this work, KIB cathode material nano-perovskite $K(Mn_{0.95}Ni_{0.05})F_3$ with concentration gradient was synthesized by EDTA-assisted homogeneous precipitation method for the first time and characterized. The solid solution material was deposited on the multi-walled carbon nanotubes (MWCNTs) to form $K(Mn_{0.95}Ni_{0.05})F_3$/MWCNT nanocomposites to improve the electron conductivity of the electrode material so as to obtain the excellent electrochemical performance. As expected, the charge and discharge capacities of $K(Mn_{0.95}Ni_{0.05})F_3$/MWCNTs after the 60th cycle can still reach 106.8 and 98.5 mAh g^{-1} over the voltage range 4.2–1.2 V vs. K/K^+ at the current density of 35 mA g^{-1}, respectively. Electrochemical performance studies showed that solid solution $K(Mn_{0.95}Ni_{0.05})F_3$ had the potential applications as the cathode material for KIBs. Electrochemical impedance spectroscopy (EIS) was used to study the transport and reaction processes of ions at the solid–liquid interface. The main factors affecting electrochemical performance could be analyzed from the Nyquist plot of the EIS test.

Keywords: Concentration-gradient structure, Electrochemistry, Homogeneous precipitation, Nanoparticles, Potassium-ion batteries

Introduction

Driven by the growing demand for portable instruments and devices, a wide range of research groups have engaged in comprehensive and in-depth research on lithium-ion batteries (LIBs) [1, 2]. The application of LIBs is limited because of the relative rarity and uneven distribution of lithium resources [3, 4]. Potassium, as the same main group and adjacent element after sodium, can provide a lower reduction potential, allowing it to be operated at higher potentials to increase the energy density. Compared with sodium-ion batteries (NIBs), potassium-ion batteries (KIBs) are less studied and still in the early stage of development, especially the cathode material [5, 6].

The critical point to develop excellent performance KIBs mainly lies in designing the rational microstructure of the cathode materials to realize the ideal insertion/extraction of K-ion. In the current application field for KIBs, vanadium-based and open framework cathode have received extensive attention due to the high-voltage platform and accommodating corresponding volume changes during the charge and discharge cycle, respectively [7–11].

From the perspective of a wide range of costs and resources, manganese-based materials have received extensive attention as electrode materials for various types of batteries, such as lithium-ion batteries [12], sodium-ion batteries [13, 14], and flow batteries [15]. Among them, manganese-based layered oxides are favored by researchers due to their high theoretical capacity [13]. However, as the cathode of KIB, manganese-based layered oxides exhibit limited capacity and a relatively low

* Correspondence: cuibin@nwu.edu.cn; zhuangquanchao@126.com
[1]Key Laboratory of Synthetic and Natural Functional Molecule of Ministry of Education, Shanxi Key Laboratory of Physico-Inorganic Chemistry, College of Chemistry and Materials Science, Northwest University, Xi'an 710127, China
[3]Li-ion Batteries Lab, School of Materials Science and Engineering, China University of Mining and Technology, Xuzhou 221116, China
Full list of author information is available at the end of the article

voltage platform, which limits their application [16]. It has been reported that representative cathode in manganese-based material $K_{0.3}MnO_2$ [17] and $K_{0.5}MnO_2$ [18] do not achieve a charging voltage higher than 4 V. In order to enrich the research of manganese-based electrode materials for KIBs, other types of manganese-based electrode materials have also received increasing attention.

Based on the resource advantages of manganese and our team's work in the study of fluoride cathode materials, we choose perovskite manganese-based fluoride as the base cathode material [19–21]. Fluorine-containing electrode materials have high pressure resistance and can alleviate the defects of low voltage platform of electrode materials [22]. The major reason to limit the application of fluorine-containing is the strong ionic bond characteristics of fluoride resulting in a wide band gap and poor electron conductivity [23]. An efficient way to facilitate the charge transfer process of the electrode material is to rationally design composites [24]. The existing methods for preparing fluoride suffer from a number of notable limitations, such as the requirement of an ultrahigh temperature, complex procedures and the usage of corrosive HF and toxic F_2 [20, 25]. The homogeneous precipitation method has been successfully applied to the preparation of other electrode materials and has achieved excellent electrochemical performance [26]. This method has the advantages of mild synthesis conditions, uniform particle size preparation and controllable morphology. Therefore, if the homogeneous precipitation method is used to synthesize a manganese-based fluoride nanomaterial, it is desirable to simultaneously solve the problem of the harsh preparation conditions and the poor conductivity. On the one hand, the fluoride with uniform particle size can effectively mix with conductive material to form a composite phase, and then improve the overall conductivity of the electrode material [27–30]. On the other hand, the effect of improving the conductivity of the material can be achieved by using more internal electron channels and tunneling effect of nanomaterials with special morphology [31, 32].

In this paper, nano-perovskite cathode material $K(Mn_{0.95}Ni_{0.05})F_3$ was synthesized by EDTA-assisted homogeneous precipitation method. EDTA acts as a buffer and chelating agent to control the release rate of Mn during precipitation [33, 34]. In addition, EDTA prevents particle coagulation by shielding the metal ions, which is another necessity for the preparation of monodispersed particles [35]. Nano-structure can increase the surface reactivity and shorten electronic and ionic pathways within particles [36–38]. To this end, nano-perovskite $K(Mn_{0.95}Ni_{0.05})F_3$ was used as the cathode for KIBs. Meanwhile, $K(Mn_{0.95}Ni_{0.05})F_3$/MWCNT nanocomposite electrode material obtained superior electrochemical performance by nano-level mixing of the active material and the conductive agent. Electrochemical impedance spectroscopy (EIS) was used to study the transport and reaction processes of ions at the solid-liquid interface.

Materials and Methods

Raw Material

The raw materials are listed as follows: $C_{10}H_{14}N_2O_8Na_2{\cdot}2H_2O$ (EDTA-2Na, 98%, Aladdin), $Mn(CH_3COO)_2{\cdot}4H_2O$ (99%, Aladdin), $Ni(CH_3COO)_2{\cdot}4H_2O$ (99.9%, Aladdin), KF (99%, Aladdin), multi-walled carbon nanotubes (MWCNTs; > 95%, Aladdin), polyvinylidene fluoride (PVDF; Arkema), and *N*-methyl pyrrolidone (NMP; 99%, Macklin).

Material syntheses

>Nano-perovskite $K(Mn_{0.95}Ni_{0.05})F_3$ was synthesized using a new synthesis method, namely EDTA-assisted homogeneous precipitation. All reagents used were of analytical grade and were used directly without any purification. The synthetic steps were shown below. Six millimoles of EDTA-2Na and 5.25 mmol of $Mn(CH_3COO)_2{\cdot}4H_2O$ were dissolved in 75 ml of water and 75 ml of ethanol, stirred and dissolved. Then, 20 mmol of KF was added and dissolved, and the resulting solution was named A. $Ni(CH_3COO)_2{\cdot}4H_2O$ (6.0 mmol, 6.25 mmol, and 6.5 mmol) was dissolved in 80 mol of water and 80 ml of ethanol and added dropwise to solution A using a dropping funnel under continuous stirring. Under the conditions of reacting for 30 min and standing for 12 h, the production was centrifuged using high-speed centrifuge (Biobase, TD-4 M, Jinan, China) to obtain a solid product Then, the solid product was washed several times with ethanol and distilled water, collected and dried at 60 °C to obtain $KMnF_3$, $K(Mn_{0.975}Ni_{0.025})F_3$ and $K(Mn_{0.95}Ni_{0.05})F_3$, respectively. The synthesis of $KMnF_3$ and $K(Mn_{0.975}Ni_{0.025})F_3$ was used to compare and verify the formation of $K(Mn_{0.95}Ni_{0.05})F_3$.

Fabrication of K(Mn0.95Ni0.05)F3/MWCNT Composite

MWCNTs (0.1 g) were added directly to 25 ml of water and ethanol (volume ratio, 1:1) at room temperature and sonicated for 0.5 h to achieve good dispersion. The dispersed carbon nanotubes were added to the solution A and stirred. The subsequent steps were performed according to the same procedure as the syntheses of $K(Mn_{0.95}Ni_{0.05})F_3$.

Material Characterization

The structure and chemical components of the products were characterized by X-ray diffraction (XRD; Bruker D8 ADVANCE with Cu Kα radiation) over an angular range of 10–70° with a step width of 0.02° (40 KV, 40 mA) and X-ray photoelectron spectroscopy (XPS; ESCALAB 250Xi with 150 W Al Ka probe beam). The morphology of the synthesized products was analyzed by field mission transmission

electron microscopy (Tecnai G2 F20). The exact element content of the prepared materials was determined by inductively coupled plasma atomic emission spectrometry (ICP-AES; Thermo Scientific iCAP 6500 Duo).

Electrochemical Characterization

To prepare working electrodes,70 wt% active material ($K(Mn_{0.95}Ni_{0.05})F_3$, $K(Mn_{0.95}Ni_{0.05})F_3$/MWCNTs), 20 wt% conductive agent, and 10 wt% PVDF binder in NMP solvent were ball-milled in a planetary ball mill (Nanjing University Instrument Factory, QM-3SP04, Nanjing, China) to achieve thorough mixing and coated on the aluminum foil. The prepared electrode film was dried under vacuum at 120 °C for 12 h. The electrolyte was 0.85 mol L^{-1} KPF_6 in ethylene carbonate (EC) and diethyl carbonate (DEC) (1:1, *v*/*v*; Mojiesi Energy Technology Co., Ltd., Nanjing, China). The button battery was assembled in a glove box with argon atmosphere (Mikrouna super 1220/750, Shanghai, China). The assembled battery was used to test the charge and discharge progress of the KIBs in the battery analyzers (Neware, Shenzhen, China) over a range of 4.2–1.2 V vs. k/k^+. EIS was tested on an electrochemical workstation (CHI660D, Chenhua Co., Ltd, Shanghai, China) using a three-electrode system with a frequency range from 10^5 to 10^{-2} Hz.

Results and Discussion

Structural and Morphological Characterization of K(Mn0.95Ni0.05)F3 Nanoparticles

XRD patterns could be used to confirm the formation of the solid solution $K(Mn_{0.95}Ni_{0.05})F_3$. Figure 1 showed the XRD pattern of the product at different nickel acetate additions. When the amount of nickel acetate added was 6 mmol, all of the nickel ions participated in the complexation reaction to form EDTA-Ni, and the product was a pure perovskite structure $KMnF_3$ (PDF 17-0116). This result confirmed that the manganese ions displaced in EDTA-Mn participate in the precipitation reaction at the beginning of the reaction. When the nickel acetate addition continued to increase to 6.25 mmol and 6.5 mmol, the diffraction peak gradually shifted to a higher angle to form $K(Mn_{0.975}Ni_{0.025})F_3$ and $K(Mn_{0.95}Ni_{0.05})F_3$, respectively. This phenomenon was mainly due to the partial substitution of Ni^{2+} with smaller ionic radius for Mn^{2+} with larger ionic radius to form a solid solution structure. ICP-AES was used to further determine the elemental ratio of manganese-cobalt in $K(Mn_{0.975}Ni_{0.025})F_3$ and $K(Mn_{0.95}Ni_{0.05})F_3$. The calculation results were close to the theoretical ratio according to the amount added in the synthesis process (Table 1).

Figure 2 showed the TEM images of $KMnF_3$, $K(Mn_{0.975}Ni_{0.025})F_3$, and $K(Mn_{0.95}Ni_{0.05})F_3$, which matched the XRD results. Since the release rate of Mn was controlled by using EDTA as a buffer and a chelating agent in the precipitation process, the prepared particles had good particle dispersion and uniform particle size. As shown in Fig. 2a, b, the product $KMnF_3$ nanoparticles showed an average size of about 150 nm and an uneven particle size distribution. As shown in Fig. 2c, d, the size average particle size of $K(Mn_{0.975}Ni_{0.025})F_3$ nanoparticles was about 120 nm, which was significantly less than $KMnF_3$ nanoparticles. As depicted in Fig. 2e, f,

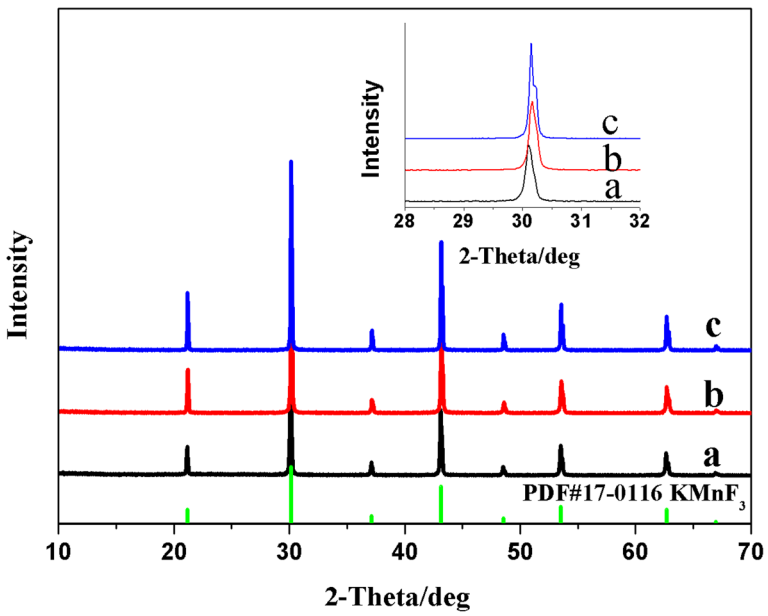

Fig. 1 The XRD patterns of $KMnF_3$ (a), $K(Mn_{0.975}Ni_{0.025})F_3$ (b), and $K(Mn_{0.95}Ni_{0.05})F_3$ (c) corresponding to different nickel acetate additions (a, b, and c represent the corresponding products when the addition of nickel acetate were 6.0 mmol, 6.25 mmol, and 6.5 mmol, respectively)

Table 1 Test results of ICP-AES of synthetic material $K(Mn_{0.975}Ni_{0.025})F_3$ and $K(Mn_{0.95}Ni_{0.05})F_3$

Electrode	Concentration of Mn/mmol L^{-1}	Concentration of Co/mmol L^{-1}	Measured molar ratio of Mn to Co	Theoretical molar ratio of Mn to Co
$K(Mn_{0.975}Ni_{0.025})F_3$	0.1289	0.0032	40.28:1	39:1
$K(Mn_{0.95}Ni_{0.05})F_3$	0.1252	0.0067	18.70:1	19:1

the uniform dispersed $K(Mn_{0.95}Ni_{0.05})F_3$ nanoparticles showed an average size of about 100 nm. What was more worth mentioning was that the reduction in particle size did not affect the retention of good dispensability. Nanoparticles with the narrow particle size distribution could improve the contact between the particles and the conductive agent and shorten the electron and ion pathways within the particles, thereby increasing the electrical conductivity. Significant contrast changes of the nanoparticles from the inside to the outside could also be seen from the TEM images.

In view of the smaller particle size and uniform particle size distribution of the solid solution structure $K(Mn_{0.95}Ni_{0.05})F_3$, it was selected as the research object for subsequent further morphological and performance characterization.

The further supplement and verification of the structure and morphology of $K(Mn_{0.95}Ni_{0.05})F_3$ was demonstrated in Fig. 3. The energy-dispersive spectrum (EDS) further verified the elemental composition and the element ratio of Mn to Ni of the synthesized nanoparticles $K(Mn_{0.95}Ni_{0.05})F_3$, as shown in Fig. 3a, b. As can be seen from Fig. 3c, the change in interplanar spacing was also used to aid in demonstrating the structure of the particles. The interplanar spacing of 0.418 nm matched the (100) crystal plane of $KMnF_3$ (PDF 17-0116), and the interplanar spacing of 0.415 nm matched the K(Mn,Ni)F_3 solid solution. In addition, elemental mapping images (d, e, f, g, h) and the line scanning curves (i, j, k, l) in Fig. 3 suggested the corresponding distribution of F, K, Mn, and Ni elements for the $K(Mn_{0.95}Ni_{0.05})F_3$ solid solution structure. As can be seen from the mapping and line scan results of Mn and Ni elements, the elemental distribution of Ni was relatively uniform, while that of Mn element was more distributed in the center of the particle, decreasing gradually from the center to the surface. The elemental distribution of Mn in nanoparticles showed the significant concentration gradient. The predicted synthesis process of the concentration-gradient structure was given in Scheme 1. At the beginning of the reaction, Mn^{2+} in EDTA-Mn was slowly replaced by Ni^{2+} and first participated in the reaction. With the increasing of the reactions, Ni^{2+} participated in the reaction and coated the surface of the particles. Ni^{2+} in the surface of the reaction prevented the diffusion of Mn^{2+} during the reaction. The difference in diffusion rate of Mn^{2+} and Ni^{2+} leaded to the formation of the concentration-gradient structure. In addition, the surface content of Ni element from the XPS tests (Additional file 1: Figure S1) was relatively higher than that of the EDS test, which was also an auxiliary proof of the concentration-gradient structure.

The special structure of K(Mn,Ni)F_3 could effectively prevent the dissolution of manganese ions in the electrolyte and improve the cycle stability of the potassium-ion

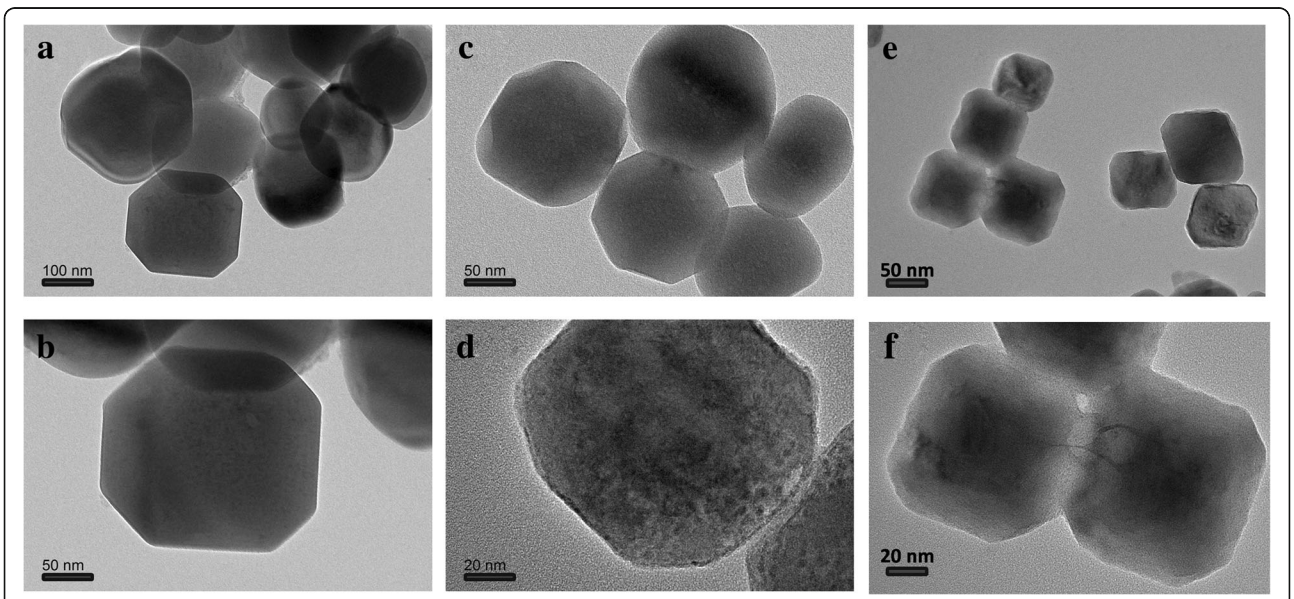

Fig. 2 TEM images of $KMnF_3$ (**a**, **b**), $K(Mn_{0.975}Ni_{0.025})F_3$ (**c**, **d**), and $K(Mn_{0.95}Ni_{0.05})F_3$ (**e**, **f**)

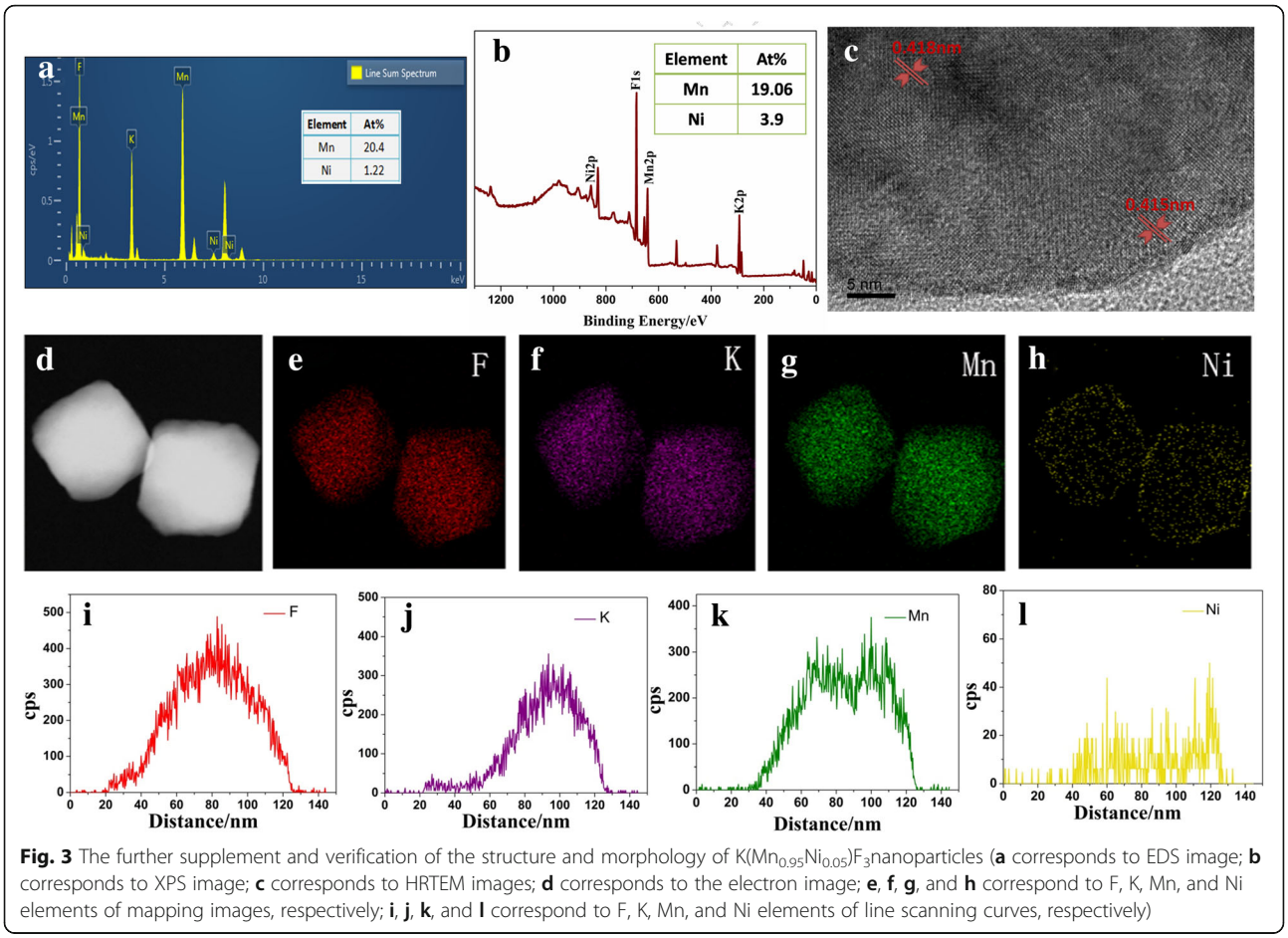

Fig. 3 The further supplement and verification of the structure and morphology of $K(Mn_{0.95}Ni_{0.05})F_3$nanoparticles (**a** corresponds to EDS image; **b** corresponds to XPS image; **c** corresponds to HRTEM images; **d** corresponds to the electron image; **e**, **f**, **g**, and **h** correspond to F, K, Mn, and Ni elements of mapping images, respectively; **i**, **j**, **k**, and **l** correspond to F, K, Mn, and Ni elements of line scanning curves, respectively)

batteries. The concentration-gradient structure could effectively realize the ion migration and electron transfer during charge–discharge, leading to superior electrochemical properties [39]. Another advantage that cannot be ignored was that the concentration-gradient structure can overcome the shortcomings of the structure mismatch in the general core–shell electrode [24].

Structural and Morphological Characterization of K(Mn0.95Ni0.05)F3/MWCNTs

In order to improve the electronic conductivity of the material, $K(Mn_{0.95}Ni_{0.05})F_3$ was deposited on the MWCNTs to obtain $K(Mn_{0.95}Ni_{0.05})F_3$/MWCNT nanocomposites so as to obtain the excellent electrochemical performance. The formation of composite structure between $K(Mn_{0.95}Ni_{0.05})F_3$ and MWCNTs was confirmed by morphology and structure analysis. In Fig. 4, it was shown that the well-dispersed $K(Mn_{0.95}Ni_{0.05})F_3$ nanoparticles formed by bonding with MWCNTs. The size of the nanoparticles $K(Mn_{0.95}Ni_{0.05})F_3$ was still around the size range of 100, making it easy to form a good combination with nano-scale MWCNTs to further improve the conductivity of the material.

The chemical composition of $K(Mn_{0.95}Ni_{0.05})F_3$/MWCNTs was analyzed by XRD and XPS, and the results were shown in Additional file 1: Figure S1. The diffraction peak around 26° can be clearly seen in the XRD pattern of the sample of $K(Mn_{0.95}Ni_{0.05})F_3$/MWCNTs (Additional file 1: Figure S1a), verifying the presence of MWCNTs in the sample (JCPDS file No. 25-0284) [40]. XPS spectra were used to characterize the composition and the state of chemical bonding of the nanocomposite structure. The broad-spectrum scan confirmed the presence of K, F, Mn, Ni, and C elements in Additional file 1: Figure S1b. Aromatic carbon in MWCNTs was the most important source of C1s peak in the survey XPS spectrum [41], as shown clearly in Additional file 1: Figure S1c. In addition to the carbon in the MWCNT matrix, functional groups containing carbon and oxygen atoms (C=O and C–O) can also be obtained in Additional file 1: Figure S1c, demonstrating the presence of surface functional groups. Primarily, the high-resolution XPS spectrum of C1s depicted in Additional file 1: Figure S1c presented the chemical bonding C-F3 and C-F4 at 293.3 and 295.9 eV [42]. The formation of these bonds confirmed that fluorine of $K(Mn_{0.95}Ni_{0.05})F_3$ was attached to the carbon of the MWCNTs, thereby facilitating the achievement of good

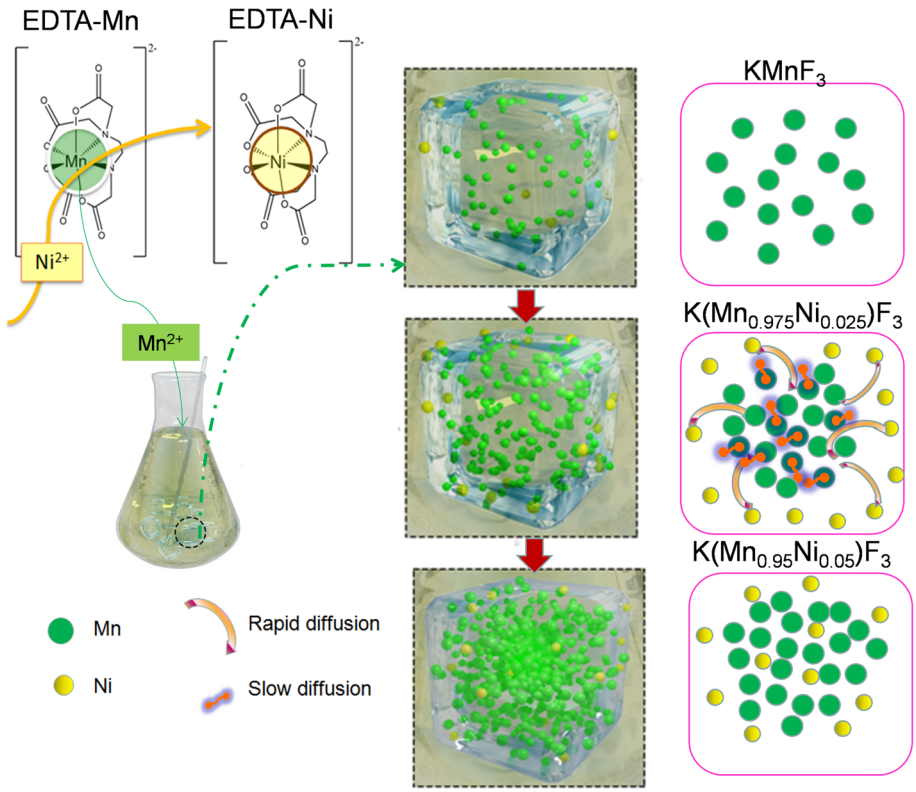

Scheme 1 Synthesis process of the concentration-gradient structure of $K(Mn_{0.95}Ni_{0.05})F_3$

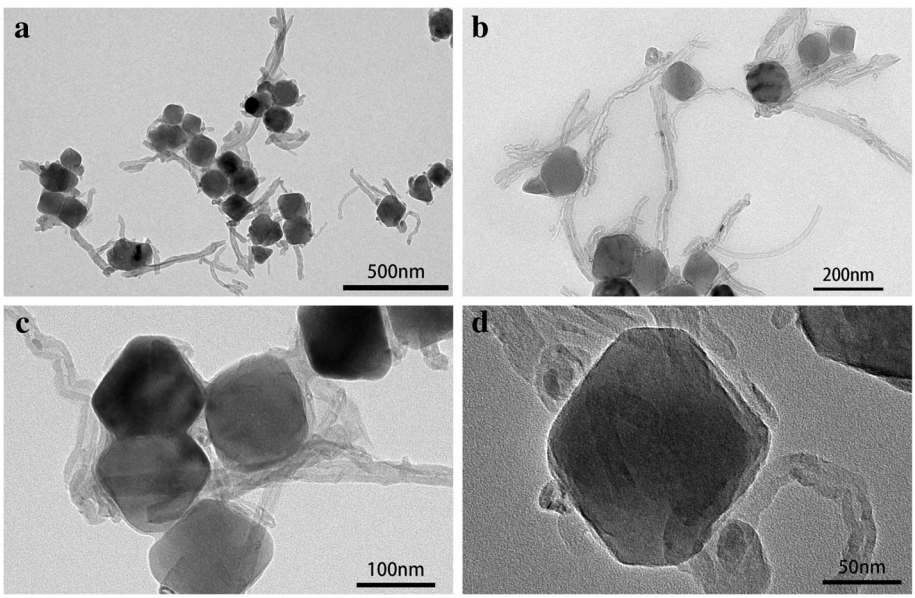

Fig. 4 a–d TEM images of $K(Mn_{0.95}Ni_{0.05})F_3$/MWCNT composites corresponding to different magnifications

electron transfer between the active material and the conductive agent. The analysis herein proved that an effective bond was produced between the carbon nanotubes and the $K(Mn_{0.95}Ni_{0.05})F_3$ by chemical bonds.

Electrochemical Performance as the Cathode of KIBs

The electrochemical performances of the as-prepared material $K(Mn_{0.95}Ni_{0.05})F_3$ and $K(Mn_{0.95}Ni_{0.05})F_3$/MWCNTs were first evaluated to demonstrate the impact of MWCNTs addition. The galvanostatic charge/discharge cycling of $K(Mn_{0.95}Ni_{0.05})F_3$ and $K(Mn_{0.95}Ni_{0.05})F_3$/MWCNTs at a current density of 35 mA g^{-1} over the voltage range 4.2–1.2 V vs. K/K^+ was shown in Fig. 5. From an overall view, the two materials exhibited high charge and discharge capacity due to better morphology control. Compared with $K(Mn_{0.95}Ni_{0.05})F_3$, the $K(Mn_{0.95}Ni_{0.05})F_3$/MWCNT electrode had a higher cycle stability and coulombic efficiency. During the first several cycles, the capacity of the $K(Mn_{0.95}Ni_{0.05})F_3$ electrode decreased monotonically, which might be ascribed to the SEI film stabilization and irreversible trapping of some potassium in the lattice [43]. Obviously, the charge–discharge capacity of $K(Mn_{0.95}Ni_{0.05})F_3$ showed obvious instability during the charge and discharge cycle, while the charge–discharge capacity of $K(Mn_{0.95}Ni_{0.05})F_3$/MWCNT material showed higher stability during 60 cycles. The charge and discharge capacities of $K(Mn_{0.95}Ni_{0.05})F_3$/MWCNTs after the 60th cycle can still reach 106.8 and 98.5 mAh g^{-1}, respectively. A high capacity retention rate of 92.6% can still be maintained after 60 cycles. Since the basic materials and test conditions of the electrodes in these experiments were the same, we conclude that the improvement of the charge–discharge capacity of the battery results from the addition of MWCNTs.

The rate performance at different current densities of 35 mA g^{-1} to 280 mA g^{-1} was used to further evaluate the rate performance of the $K(Mn_{0.95}Ni_{0.05})F_3$/MWCNT cathode in the voltage range of 4.2–1.2 V. As shown in Additional file 1: Figure S2 a, the battery exhibited excellent cycle performance when the current density experienced different current

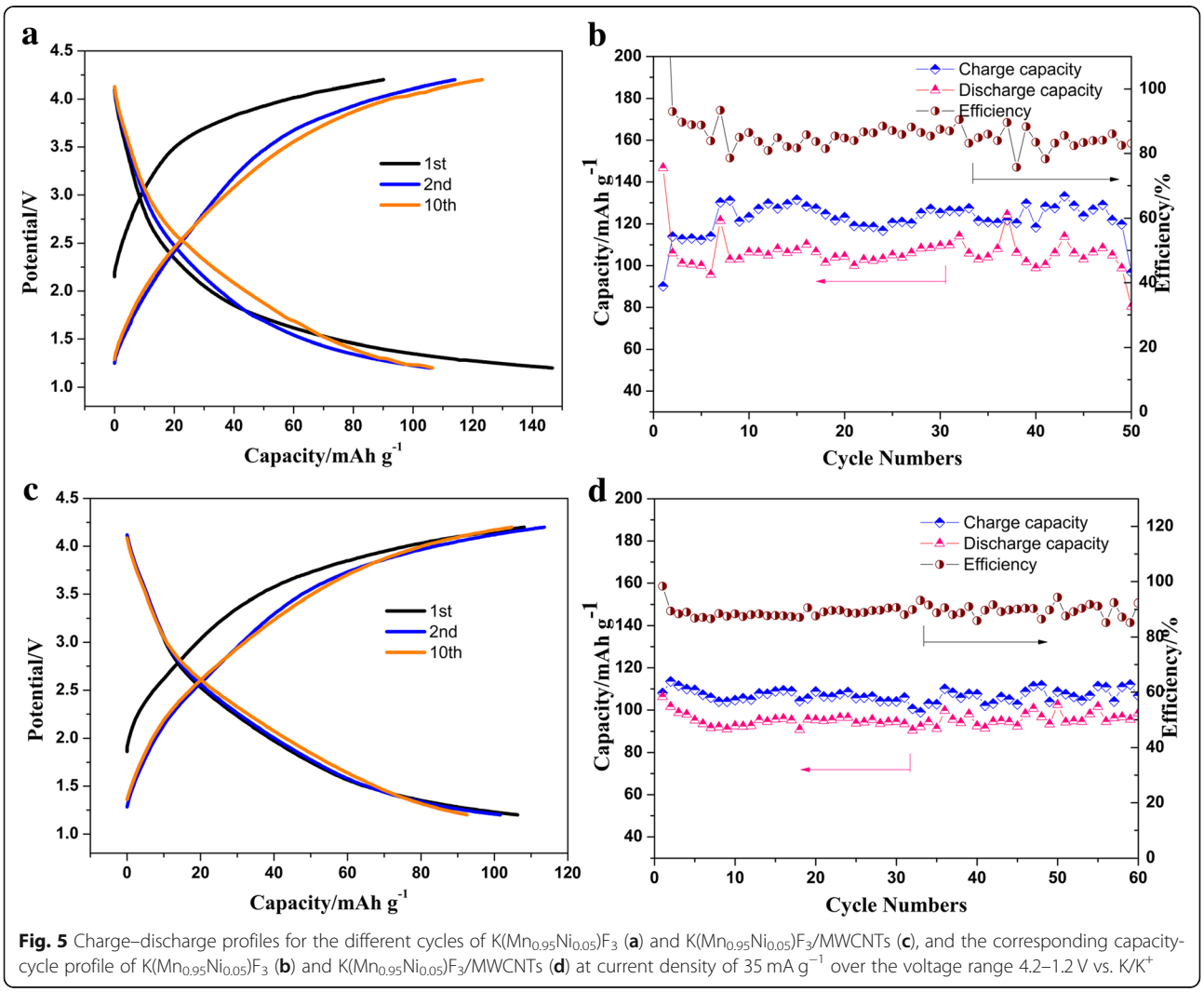

Fig. 5 Charge–discharge profiles for the different cycles of $K(Mn_{0.95}Ni_{0.05})F_3$ (**a**) and $K(Mn_{0.95}Ni_{0.05})F_3$/MWCNTs (**c**), and the corresponding capacity-cycle profile of $K(Mn_{0.95}Ni_{0.05})F_3$ (**b**) and $K(Mn_{0.95}Ni_{0.05})F_3$/MWCNTs (**d**) at current density of 35 mA g^{-1} over the voltage range 4.2–1.2 V vs. K/K^+

densities. Additional file 1: Figure S2b presented the CV curves of $K(Mn_{0.95}Ni_{0.05})F_3$/MWCNT cathode at 0.2 mV s^{-1}. The obtained CV curve was basically consistent with the charge and discharge process and also had the same characteristics as the CV curve of the sodium-ion battery of such materials. The CV curves were almost overlapped, implying the superior reversibility during deintercalation/intercalation process of K-ions.

Electrochemical Impedance Spectroscopy of Synthetic Materials

To investigate the interfacial reaction process of $K(Mn_{0.95}Ni_{0.05})F_3$/MWCNT composites at the electrode/electrolyte interface, EIS measurements of $K(Mn_{0.95}Ni_{0.05})F_3$/MWCNT composite electrodes were performed during the first charge and discharge process (Fig. 6 and Additional file 1: Figure S3). Under the open circuit potential, the Nyquist plots of $K(Mn_{0.95}Ni_{0.05})F_3$/MWCNTs during the first charge seem to consist of three components, namely, the high-frequency semicircle (HFS), the mid-frequency semicircle (MFS), and the mid-low frequency line or arc (MLFL/A). During the continuous increase of voltage to the end of charging and subsequent discharge, HFS and MFS were always present and did not change much. HFS was generally attributed to a semicircle associated with the formation of the SEI film. Combined with the charge and discharge process, it was known that the formation of the SEI film hardly occurred during the first cycle of charging, but occurred during the standing process before the charging process. The impedance spectrum after standing could prove the conclusion that the SEI film was formed at this stage (Additional file 1: Figure S4). This indicated that it was reasonable to have a semicircle associated with the SEI film at the open circuit voltage of the first cycle, and there would be no significant change during charging. This phenomenon further proved that HFS can be attributed to the migration of potassium-ion through SEI film [44]. The stable presence of the SEI film was one of the main reasons for the charge and discharge cycle stability of the composite electrode. According to the previous literature on fluoride EIS research [19], the MFS should be related to the Schottky contact between fluoride and conductive agents,

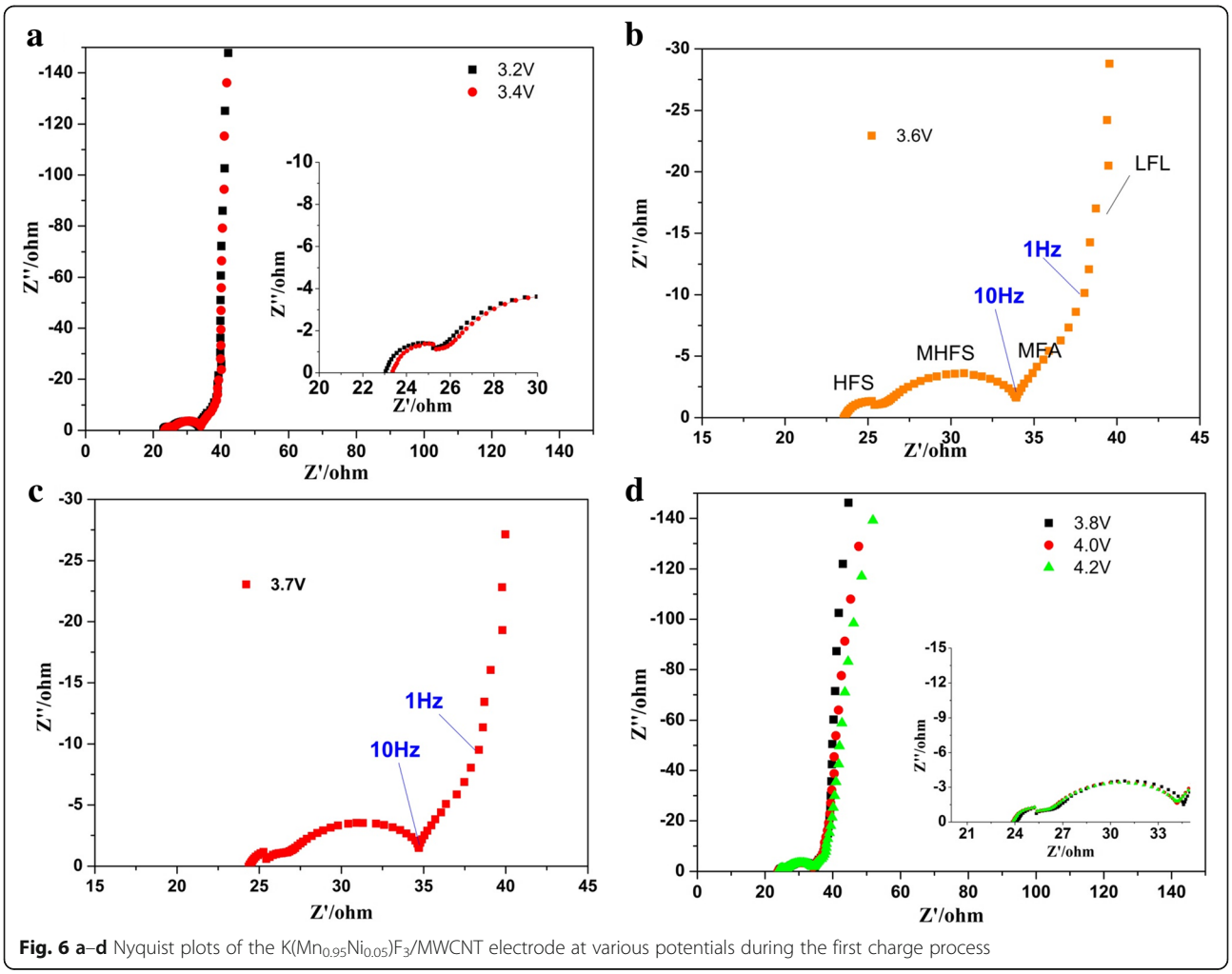

Fig. 6 a–d Nyquist plots of the $K(Mn_{0.95}Ni_{0.05})F_3$/MWCNT electrode at various potentials during the first charge process

which may be the important feature of such composite materials with the big band gap. Therefore, we can basically determine that MFS was related to electron conductivity. Combined with the frequency data given in Fig. 6b, c, it could be demonstrated that the cathode semicircle at several Hz (MLF) should be attributed to charge transfer [45]. The lower conductivity of the fluoride electrode resulted in a higher charge transfer resistance, so the semicircle of the mid-low frequency region only appeared as the line or arc. As the potential increased during charging, the low frequency region associated with the charge transfer process did not show the significant tendency to bend to form a circular arc, primarily due to the high charge transfer resistance [45–47]. Based on the above analysis, the three components that appear on the EIS spectrum were related to the SEI film, electron conductivity, and charge transfer resistance, respectively. The equivalent circuit for fitting the corresponding EIS diagram was shown in Additional file 1: Figure S5 and had typical characteristics of an equivalent circuit of a fluoride electrode material [48]. R_s stands for solution resistance, R_1, R_2, and R_3, and constant phase angle elements (CPE; Q_1, Q_2, and Q_3) represent the related resistors and capacitors of HFS, MFS, and LFS, respectively.

The Nyquist plots comparison of $K(Mn_{0.95}Ni_{0.05})F_3$ and $K(Mn_{0.95}Ni_{0.05})F_3$/MWCNT cathode at the first charge to 4.0 V was shown in Additional file 1: Figure S6. In the Nyquist diagram of $KMnF_3$ to Ni^{2+}/MWCNTs, the bending tendency of the oblique line in the MLF region representing the charge transfer process would be more pronounced. This also verified that the addition of MWCNTs improved the electrochemical activity of the positive electrode material to a certain extent, thereby improving the electrochemical performance. Since the region representing the charge transfer resistance still failed to bend into a semicircle, the charge transfer resistance might still be an important parameter affecting the electrochemical performance of the synthesized fluoride material.

Conclusions

In summary, we reported the synthesis of concentration-gradient structure material $K(Mn_{0.95}Ni_{0.05})F_3$ and $K(Mn_{0.95}Ni_{0.05})F_3$/MWCNTs as cathode materials for KIBs. $K(Mn_{0.95}Ni_{0.05})F_3$ was synthesized by EDTA-assisted homogeneous precipitation method for the first time, and the formation process of concentration gradient of the material was predicted. This approach to prepare concentration-gradient structure fluoride cathode can be further extended to design other nano-structure systems for electrode material. On this basis, $K(Mn_{0.95}Ni_{0.05})F_3$ was deposited on the MWCNTs to improve the electron conductivity of the material so as to obtain the electrode material with more excellent electrochemical performance, such as charge–discharge capacity and cycle stability. As expected, the $K(Mn_{0.95}Ni_{0.05})F_3$/MWCNT composite electrode exhibited superb cycling stability. The charge and discharge capacities of $K(Mn_{0.95}Ni_{0.05})F_3$/MWCNTs after the 60th cycle can still reach 106.8 and 98.5 mAh g^{-1} over the voltage range 4.2–1.2 V vs. K/K^+ at the current density of 35 mA g^{-1}. The Nyquist diagram of $K(Mn_{0.95}Ni_{0.05})F_3$/MWCNT composite electrode revealed that charge transfer resistance might be an important parameter affecting the electrochemical performance of the synthetic fluoride material.

Additional file

Additional file 1: Figure S1. $K(Mn_{0.95}Ni_{0.05})F_3$/MWCNT composites. (a) XRD pattern, (b) XPS survey spectrum, (c) high-resolution XPS spectrum of C1s. **Figure S2.** Rate performance (a) and CV curves (b) of $K(Mn_{0.95}Ni_{0.05})F_3$/MWCNTs as the cathode over the voltage range 4.4–1.2 V vs. K/K^+. **Figure S3.** Nyquist plots of the $K(Mn_{0.95}Ni_{0.05})F_3$/MWCNT electrode at various potentials during the first discharge process. **Figure S4.** Nyquist plots of the $K(Mn_{0.95}Ni_{0.05})F_3$/MWCNT electrode at Open circuit potential. **Figure S5.** Equivalent circuit of $K(Mn_{0.95}Ni_{0.05})F_3$/MWCNT cathode during the first charge and discharge process. **Figure S6.** Nyquist plots of $K(Mn_{0.95}Ni_{0.05})F_3$ and $K(Mn_{0.95}Ni_{0.05})F_3$/MWCNT cathode at the first charge to 4.0 V. (ZIP 4678 kb)

Abbreviations

CPE: Constant phase angle elements; DEC: Diethyl carbonate; EC: Ethylene carbonate; EDS: Energy-dispersive spectrum; EIS: Electrochemical impedance spectroscopy; HFS: High-frequency semicircle; ICP-AES: Inductively coupled plasma atomic emission spectrometry; KIBs: Potassium-ion batteries; LIBs: Lithium-ion batteries; MFS: Mid-frequency semicircle; MLFL/A: Mid-low frequency line or arc; MWCNTs: Multi-walled carbon nanotubes; NIBs: Sodium-ion batteries; NMP: *N*-Methyl pyrrolidinone; PVDF: Polyvinylidene fluoride; TEM: Transmission electron microscopy; XRD: X-ray diffraction

Acknowledgements

A special acknowledgment to Shuxuan Wang and Bo Li from Qinghai Institute of Salt Lakes, Chinese Academy of Sciences for their suggestions and guidance in the revision of the paper.

Authors' Contributions

SW, BC, and HZ designed the experiments of material synthesis. SW performed the experiments and analyzed the data. QZ and YS guided the analysis of electrochemical performance data. QZ and BC reviewed and edited the manuscript. XZ modify and improve the grammar of the manuscript and guide the revision. All authors read and approved the final manuscript.

Funding

This work was supported by National Natural Science Foundation of China (U1730136) and the Fundamental Research Funds for the Central Universities (2017XKQY062).

Availability of Data and Materials

The data supporting the conclusions of this article are included within the article.

Ethics Approval and Consent to Participate

Not applicable.

Competing Interests

The authors declare that they have no competing interests.

Author details

[1]Key Laboratory of Synthetic and Natural Functional Molecule of Ministry of Education, Shanxi Key Laboratory of Physico-Inorganic Chemistry, College of Chemistry and Materials Science, Northwest University, Xi'an 710127, China. [2]Qinghai Engineering and Technology Research Center of Comprehensive Utilization of Salt Lake Resources, Qinghai Institute of Salt Lakes, Chinese Academy of Sciences, Xining 810008, China. [3]Li-ion Batteries Lab, School of Materials Science and Engineering, China University of Mining and

Technology, Xuzhou 221116, China. [4]Department of Chemistry, Chongqing Normal University, Chongqing 401331, China.

Received: 22 March 2019 Accepted: 19 June 2019
Published online: 16 July 2019

References

1. Chen W, Qian T, Xiong J, Xu N, Liu X, Liu J, Zhou J, Shen X, Yang T, Chen Y, Cs Y (2017) A new type of multifunctional polar binder: toward practical application of high energy lithium sulfur batteries. *Adv. Mater.* 29:1605160
2. Nicolau BG, Petronico A, Letchworth-Weaver K, Ghadar Y, Haasch RT, Soares JANT, Rooney RT, Chan MKY, Gewirth AA, Nuzzo RG (2018) Controlling interfacial properties of lithium-ion battery cathodes with alkylphosphonate self-assembled monolayers. *Adv. Mater. Interfaces* 5:1701292
3. Zhang Y, Guo Y, Wang Y, Peng T, Lu Y, Luo R, Wang Y, Liu X, Kim JK, Luo Y (2018) Rational design of 3D honeycomb-like SnS 2 quantum dots/rGO composites as high-performance anode materials for lithium/sodium-ion batteries. *Nanoscale Res. Lett.* 13:389
4. Youn DH, Choi YH, Kim J-H, Han S, Heller A, Mullins CB (2018) Simple microwave-assisted synthesis of delafossite CuFeO2 as an anode material for sodium-ion batteries. *ChemElectroChem* 5:2419–2423
5. Sultana I, Ramireddy T, Rahman MM, Chen Y, Glushenkov AM (2016) Tin-based composite anodes for potassium-ion batteries. *Chem. Commun. (Camb).* 52:9279–9282
6. Kim H, Kim JC, Bo S-H, Shi T, Kwon D-H, Ceder G (2017) K-ion batteries based on a P2-type K0.6CoO2 Cathode. *Adv. Energy Mater.* 7:1700098
7. Park WB, Han SC, Park C, Hong SU, Han U, Singh SP, Jung YH, Ahn D, Sohn K-S, Ms P (2018) KVP2O7 as a robust high-energy cathode for potassium-ion batteries: pinpointed by a full screening of the inorganic registry under specific search conditions. *Adv. Energy Mater.* 8:1703099
8. Nikitina VA, Kuzovchikov SM, Fedotov SS, Khasanova NR, Abakumov AM, Antipov EV (2017) Effect of the electrode/electrolyte interface structure on the potassium-ion diffusional and charge transfer rates: towards a high voltage potassium-ion battery. *Electrochim. Acta* 258:814–824
9. Padigi P, Thiebes J, Swan M, Goncher G, Evans D, Solanki R (2015) Prussian green: a high rate capacity cathode for potassium ion batteries. *Electrochim. Acta* 166:32–39
10. Chong S, Chen YZ, Zheng Y, Tan Q, Shu C, Liu Y, Guo Z, Chong S, Chen YZ, Zheng Y (2017) Potassium ferrous ferricyanide nanoparticles as high capacity and ultralong life cathode material for nonaqueous potassium-ion batteries. *J. Mater. Chem. A* 5:22465–22471
11. Baioun A, Kellawi H, Falah A (2018) Nano prussian yellow film modified electrode: a cathode material for aqueous potassium ion secondary battery with zinc anode. *Curr. Nanosci.* 14:227–233
12. Liu DH, Li WH, Zheng YP, Cui Z, Yan X, Liu DS, Wang J, Zhang Y, Lü HY, Bai FY (2018) In situ encapsulating α-MnS into N,S-codoped nanotube-like carbon as advanced anode material: α → β phase transition promoted cycling stability and superior li/na-storage performance in half/full cells. *Adv. Mater.*. 30:1706317
13. Liu DS, Liu DH, Hou BH, Wang YY, Guo JZ, Ning QL, Wu XL (2018) 1D porous MnO@N-doped carbon nanotubes with improved Li-storage properties as advanced anode material for lithium-ion batteries. *Electrochim. Acta*. 264:292–300
14. Yang Q, Wang PF, Guo JZ, Chen ZM, Pang WL, Huang KC, Guo YG, Wu XL, Zhang JP (2018) Advanced P2-Na2/3Ni1/3Mn7/12Fe1/12O2 Cathode material with suppressed P2-O2 phase transition toward high-performance sodium-ion battery. *ACS Appl. Mater. Interfaces* 10:34272–34282
15. Ma Q, Deng Q, Sheng H, Ling W, Wang HR, Jiao HW, Wu XW, Zhou WX, Zeng XX, Yin YX, Guo YG (2018) High electro-catalytic graphite felt/MnO2 composite electrodes for vanadium redox flow batteries. *Sci China-Chem.* 61:732–738
16. Zhang Q, Wang Z, Zhang S, Zhou T, Mao J, Guo Z (2018) Cathode materials for potassium-ion batteries: current status and perspective. *Electrochemical Energy Reviews*. 1:625–658
17. Vaalma C, Giffin GA, Buchholz D, Passerini S (2016) Non-aqueous K-ion battery based on layered K0. 3MnO2 and hard carbon/carbon black. *J. Electrochem. Soc.* 163:A1295–A1299
18. Kim H, Seo DH, Kim JC, Bo SH, Liu L, Shi T, Ceder G (2017) investigation of potassium storage in layered P3-Type K0.5 MnO2 cathode. *Adv. Mater.* 29: 1702480
19. Shi YL, Shen MF, Xu SD, Qiu XY, Jiang L, Qiang YH, Zhuang QC, Sun SG (2011) Electrochemical impedance spectroscopic study of the electronic and ionic transport properties of NiF2/C composites. *Int. J. Electrochem. Sci.* 6:3399–3415
20. Shi Y, Sun S, Liu J, Cui YL, Zhuang QC, Xs C (2016) Enhanced charge storage of Li3FeF6 with carbon nanotubes for lithium-ion batteries. *Rsc Adv.* 6:61–66
21. Sun SB, Shi YL, Bian SL, Zhuang QC, Liu MQ, Cui YH (2017) Enhanced charge storage of Na3FeF6 with carbon nanotubes for lithium-ion batteries. *Solid State Ionics*. 312:61–66
22. Guo JZ, Wang PF, Wu XL, Zhang XH, Yan Q, Chen H, Zhang JP, Guo YG (2017) High-energy/power and low-temperature cathode for sodium-ion batteries: in situ XRD study and superior full-cell performance. *Advanced Materials*. 29:1701968
23. Wang F, Robert R, Chernova NA, Pereira N, Omenya F, Badway F, Hua X, Ruotolo M, Zhang R, Wu L (2011) Conversion reaction mechanisms in lithium ion batteries: study of the binary metal fluoride electrodes. *J. Am. Chem. Soc.* 133:18828–18836
24. Hou P, Zhang H, Zi Z, Zhang L, Xu X (2017) Core–shell and concentration-gradient cathodes prepared via co-precipitation reaction for advanced lithium-ion batteries. *J. Mater. Chem. A* 5:4254–4279
25. Rüdiger S, Eltanany G, Groß U, Kemnitz E (2007) Real sol-gel synthesis of catalytically active aluminium fluoride. *J. Sol-Gel Sci. Technol.* 41:299–311
26. Jiang S, Zhang Z, Wang X, Qu Y, Lai Y, Li J (2013) Synthesis of sulfur/activated carbon aerogels composite with a novel homogeneous precipitation method as cathode materials for lithium–sulfur batteries. *Rsc Adv.* 3:16318–16321
27. Ali G, Lee JH, Cho BW, Nam KW, Ahn D, Chang W, Si HO, Chung KY (2016) Probing the sodiation-desodiation reactions in nano-sized iron fluoride cathode. *Electrochim. Acta*. 191:307–316
28. Kim SW, Seo DH, Gwon H, Kim J, Kang K (2010) Fabrication of FeF3 nanoflowers on CNT branches and their application to high power lithium rechargeable batteries. *Adv. Mater.* 22:5260–5264
29. Shi Y-L, Wu N, Shen M-F, Cui Y-L, Jiang L, Qiang Y-H, Zhuang Q-C (2014) Electrochemical behavior of iron(III) fluoride trihydrate as a cathode in lithium-ion batteries. *ChemElectroChem*. 1:645–654
30. Yang YA, Chen C, Hs S (2019) LiVPO4F@C particles anchored on boron-doped graphene sheets with outstanding Li+ storage performance for high-voltage Li-ion battery. *Solid State Ionics*. 331:6–11
31. Li T, Li L, Cao YL, Ai XP, Yang HX (2010) Reversible three-electron redox behaviors of FeF3 nanocrystals as high-capacity cathode-active materials for li-ion batteries. *J. Phys. Chem. C*. 114:3190–3195
32. Liu L, Zhou M, Wang X, Yang Z, Tian F, Wang X (2012) Synthesis and electrochemical performance of spherical FeF3/ACMB composite as cathode material for lithium-ion batteries. *J. Mater. Sci.* 47:1819–1824
33. Goderski S, Runowski M, Lis S (2016) Synthesis of luminescent KY_3F_(10) nanopowder multi-doped with lanthanide ions by a co-precipitation method. *J. Rare Earths* 34:808–813
34. Na Z, Zhang X, Shi E, Zhao S, Jiang K, Di W, Wang P, Guo S, Ping H, Zhou H (2018) In situ X-ray diffraction and thermal analysis of LiNi 0.8 Co 0.15 Al 0.05 O 2 synthesized via co-precipitation method. *J. Energy Chem.* 27:1655–1660
35. Yi G, Lu H, Zhao S, Ge Y, Yang W, Chen D, Guo LH (2004) Synthesis, characterization, and biological application of size-controlled nanocrystalline NaYF4:Yb,er infrared-to-visible up-conversion phosphors. *Nano Lett.* 4:2191–2196
36. Li C, Gu L, Tsukimoto S, van Aken PA, Maier J (2010) Low-temperature ionic-liquid-based synthesis of nanostructured iron-based fluoride cathodes for lithium batteries. *Adv. Mater.*. 22:3650–3654
37. Bruce PG, Scrosati B, Tarascon JM (2008) Nanomaterials for rechargeable lithium batteries. *Angew. Chem., Int. Ed.* 47:2930–2946
38. Lu L, Li S, Li J, Lan L, Lu Y, Xu S, Huang S, Pan C, Zhao F (2019) High-performance cathode material of FeF3·0.33H2O modified with carbon nanotubes and graphene for lithium-ion batteries. *Nanoscale Res. Lett.* 14:100
39. Song D, Hou P, Wang X, Shi X, Zhang L (2015) Understanding the origin of enhanced performances in core-shell and concentration-gradient layered oxide cathode materials. *ACS Appl. Mater. Interfaces* 7:12864
40. Dalal M, Greneche JM, Satpati B, Ghzaiel TB, Mazaleyrat F, Ningthoujam RS, Chakrabarti PK (2017) Microwave absorption and the magnetic hyperthermia applications of Li0.3Zn0.3Co0.1Fe2.3O4 nanoparticles in multi-walled carbon nanotubes matrix. *ACS Appl. Mater. Interfaces* 9:40831–40845
41. Bi H, Li Y, Liu S, Guo P, Wei Z, Lv C, Zhang J, Zhao XS (2012) Carbon-nanotube-modified glassy carbon electrode for simultaneous determination of dopamine, ascorbic acid and uric acid: The effect of functional groups. *Sens. Actuators* 171–172:1132–1140

42. Dementjev AP, Eletskii AV, Maslakov KI, Rakov EG, Sukhoverhov VF, Naumkin AV (2006) Fluorination of carbon nanostructures and their comparative investigation by XPS and XAES spectroscopy. *Fullerene Sci. Technol.* 14:287–296
43. Dong S, Li C, Ge X, Li Z, Miao X, Ls Y (2017) ZnS-Sb2S3@C Core-double shell polyhedron structure derived from metal-organic framework as anodes for high performance sodium ion batteries. *Acs Nano*. 11:6474–6482
44. Zhuang QC, Wei T, Du LL, Cui YL, Fang L, Sun SG (2010) An electrochemical impedance spectroscopic study of the electronic and ionic transport properties of spinel LiMn2O4. J. Phys. Chem. C 114:8614–8621
45. Nara H, Mukoyama D, Yokoshima T, Momma T, Osaka T (2016) Impedance analysis with transmission line model for reaction distribution in a pouch type lithium-ion battery by using micro reference electrode. *J. Electrochem. Soc.* 163:A434–A441
46. Nara H, Morita K, Mukoyama D, Yokoshima T, Momma T, Osaka T (2017) Impedance analysis of LiNi1/3Mn1/3Co1/3O2 cathodes with different secondary-particle size distribution in lithium-ion battery. *Electrochim. Acta* 241:323–330
47. Holzapfel M, Martinent A, Alloin F, Gorrec BL, Yazami R, Montella C (2003) First lithiation and charge/discharge cycles of graphite materials, investigated by electrochemical impedance spectroscopy. *J. Electroanal. Chem.* 546:41–50
48. Shi YL, Shen MF, Xu SD, Qiu XY, Jiang L, Qiang YH, Zhuang QC, Sun SG (2011) Electrochemical impedance spectroscopic study of the electronic and ionic transport properties of NiF(2)/C composites. *Int. J. Electrochem. Sci.* 6:3399–3415

Publisher's Note